First-principles study of the new potential photovoltaic absorber: Cu_2MgSnS_4 compound

Belmorsli Bekki, Kadda Amara†, and Mohammed El Keurti

Laboratoire d'étude physico-chimique, Université Dr. Moulay Tahar de Saida, 20000 Saida, Algeria

(Received 12 March 2017; revised manuscript received 28 March 2017; published online 6 June 2017)

The structural, electronic, optical, and elastic properties of Cu2MgSnS4 in four crystalline phases (wurtzite–stannite (WS), stannite (ST), kesterite (KS), and primitive-mixed CuAu (PMCA)) are investigated using density functional theory (DFT) in the framework of the full potential linearized augmented plane wave plus local-orbitals (FP-LAPW+lo) method within the generalized gradient approximation based on the Perdew 2008 functional (GGA-PBEsol). For each phase, the structural parameters, bulk modulus, and its pressure derivative are calculated. The relative stability of these phases is also discussed. In addition, the elastic constants have been calculated in order to investigate the mechanical stability of all phases. Moreover, the anisotropy factor, shear modulus, Young's modulus, Lame's coefficient, and Poisson's ratio have been estimated from the calculated single crystalline elastic constants. For the band structure, the density of states and optical properties of the exchange and correlation effects are treated by the Tran–Blaha modified Becke–Johnson potential to give a better description of the band-gap energies and optical spectra. The obtained results are compared with available experimental data and to other theoretical calculations.

Keywords: quaternary chalcogenide semiconductor, elastic constants, electronic properties, optical properties

PACS: 62.20.de, 71.20.–b, 78.20.–e, 71.15.Mb **DOI:** 10.1088/1674-1056/26/7/076201

1. Introduction

The chalcogenide semiconductors of the quaternary type (I_2–II–IV–VI_4) have gained growing attention in recent years due to their huge variety of possible compositions, which allows them to have numerous technologically useful properties as tunable semiconductors,[1–4] photovoltaics,[1,5,6] spintronics,[7,8] non-linear optics,[9,10] and thermoelectrics.[2,11,12] These compounds can be considered to be derived from either zincblende (ZB) or wurtzite (WZ) binary II–VI chalcogenides through the sequential cation cross-substitutions.[13–15] From their differences in the anion matrices, all derived structures can be split into two classes, i.e., ZB derivatives and WZ derivatives. Although the local charge around each anion always satisfies the octet rule in the element-substitution design of I_2–II–IV–VI_4 compounds, the mutations to the quaternary structures do not affect the tetrahedrally coordinated lattice framework of ZB or WZ. These structures can have a variety of cation ordering schemes with different space group symmetries. Among these crystal structures, five main structures have been reported with the smallest primitive cells and a lower energy,[14,15] namely stannite (ST), kesterite (KS), primitive-mixed CuAu (PMCA), wurtzite stannite (WS) and wurtzite kesterite (WK). The Cu-based quaternary chalcogenide compounds, Cu_2–II–IV–VI_4, can be designed for II = Zn, Cd, Hg, Mg, Ca, Sr, Ba, IV = Si, Ge, Sn, Ti, Zr, Hf, and VI = S, Se, Te due to their large compositional flexibility. Indeed, many of them have been proposed theoretically or experimentally.[16–26]

Recently, Cu_2MgSnS_4 nanocrystals have been synthesized by hot-injection methods, where it was found that this compound crystallizes in the tetragonal structure space group $I\bar{4}$.[27] In the same work, the optical band gap of this compound was measured by UV-vis absorption spectroscopy and gained a value of 1.63 eV, which is suitable for applications in the field of photovoltaic cells.[27] It is also synthesized in thin films by a new ultrasonic co-pulverization method, which shows its resemblance to the tetragonal structure and gives a measured optical band deviation of 1.76 eV.[28] More recently, induced effects by the substitution of Zn in Cu_2ZnSnX_4 (X = S and Se) have been investigated[29] by using first-principles calculations and combining them with the Heyd–Scuseria–Ernzerhof (HSE06) screened hybrid functional approximation, and for the Cu_2MgSnS_4 compound a fundamental band gap value of 1.80 eV was obtained. The lack or scarcity of work and physical data in the literature for this compound has motivated us to investigate its structural, elastic, electronic, and optical properties in the KS (space group $I\bar{4}$), ST (space group $I\bar{4}2m$), PMCA (space group $P\bar{4}2m$), and WS (space group $Pmn21$) structures, where the first structure has an orthorhombic unit cell and the last three structures have tetragonal unit cells.

Therefore, in this paper, we report the calculation results performed by means of the state-of-the-art *ab initio* self-consistent full potential linearized augmented plane wave plus local-orbitals (FP-LAPW+lo) method within the generalized gradient approximation based on the Perdew 2008 functional

†Corresponding author. E-mail: kamaraphy@gmail.com

© 2017 Chinese Physical Society and IOP Publishing Ltd

(GGA-PBEsol).[30] Furthermore, the density of states, band structure, and optical properties have been obtained using the modified Becke–Johnson potential (TB-mBJ)[31,32] which allows one to give a better description of the band-gap energies and optical spectra.

2. Computational details

First-principles calculations based on density functional theory (DFT) are carried out by using the FP-LAPW+lo method as implemented in the Wien2k code.[33] In this approach, the wave function, charge density, and potential are expanded differently in two regions of the unit cell. Inside the non-overlapping spheres of the muffin-tin (MT) radius, RMT, around each atom, which are taken to be 2.1, 1.85, 2.38, and 1.9 for Cu, Mg, Sn and S atoms, respectively, the basis set was split into core and valence subsets. The core states were treated within the spherical part of the potential only and were assumed to have a spherically symmetric charge density confined inside the MT spheres. The valence part was treated with the potential expanded in spherical harmonics to $l = 4$. The valence wave functions inside the spheres were expanded to $l = 10$ and a plane wave expansion was used in the interstitial region. To ensure convergence with minimal calculations, we tested the convergence of energy according to the k-points and the energy cut-off $R_{\mathrm{mt}}K_{\mathrm{max}}$. A test was first made using experimental Cu_2MgSnS_4 unit cell parameters to determine the number of k-points required. Figure 1(a) illustrates the variation in the energies of the Cu_2MgSnS_4 unit cell as a function of the k-points. Above 512 k-points and up to 2048 k-points, the changes in the energies with the number of k-points were about 40 μRy. It is important to check the convergence of the crystal energy as a function of $R_{\mathrm{mt}}K_{\mathrm{max}}$, the product of the smallest atomic sphere radius (R_{mt}) and the magnitude of the largest k vector in the plane wave expansion (K_{max}). With 512 k-points, $R_{\mathrm{mt}}K_{\mathrm{max}}$ was varied within the range of 6.0–9.5 with a step size of 0.5. Figure 1(b) illustrates the variation in the crystal energy as a function of $R_{\mathrm{mt}}K_{\mathrm{max}}$. It can be seen that the value $R_{\mathrm{mt}}K_{\mathrm{max}} = 8$ is enough in the calculations without being very time-consuming. Then, with a sufficient number of the plane wave function for $R_{\mathrm{mt}}K_{\mathrm{max}} = 8$, and by using 512 k-points corresponding to an $8 \times 8 \times 8$ grid for KS, ST, and PMCA, and $7 \times 8 \times 9$ grid for WS, 10^{-5} Ry, and 10^{-4} e as the convergence criterion for the total energy and the charge, respectively, were reached within 13–21 iterations for self-consistency of the charge densities.

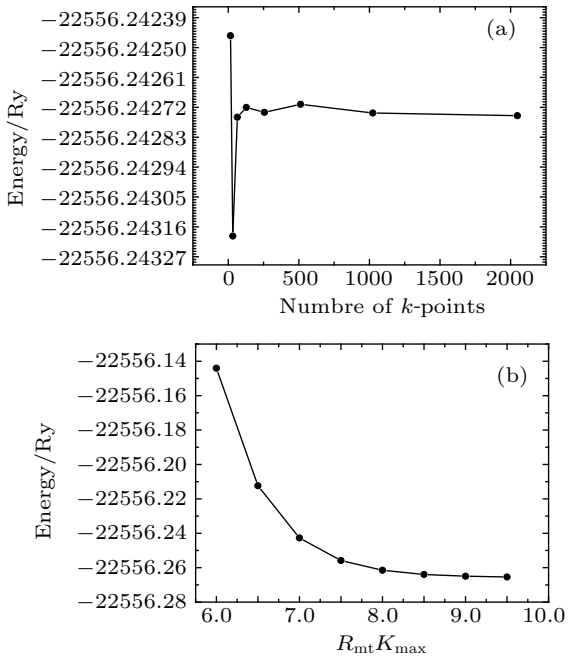


Fig. 1. Convergence test of energy according to (a) k-points and (b) $R_{\mathrm{mt}}K_{\mathrm{max}}$.

3. Results and discussion

3.1. Structural properties and phase stability

The crystal structures of the Cu_2MgSnS_4 compound are shown in Fig. 2. All structures have similar tetrahedral bond geometries where each anion atom is surrounded by two Cu atoms, one Mg, and one Sn atom. The Sn atom is bonded to four S atoms. The KS structure is characterized by alternating cation layers of CuSn, CuMg, CuSn, and CuMg at $z = 0$, $1/4$, $1/2$, and $3/4$, respectively (Fig. 2(a)). On the

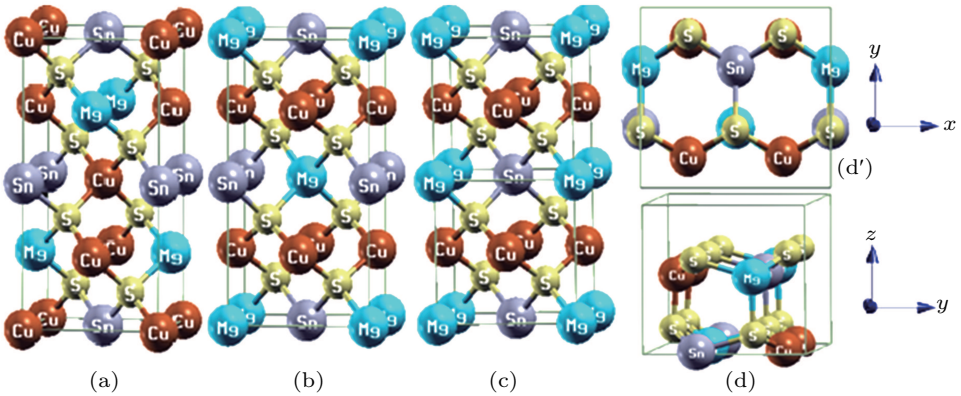


Fig. 2. (color online) Crystal structures of Cu_2MgSnS_4 in four phases (a) KS, (b) ST, (c) PMCA, and (d, d′) WS.

other hand, in the ST structure MgSn layers alternate with Cu_2 layers (Fig. 2(b)). In both structures, the Sn is located at the same structural site. The PMCA structure with two unit cells shown in Fig. 2(c) was obtained from the ST structure by interchanging the Mg and Sn atoms positions in the $z = 1/2$ MgSn layer. In the WS structure, the atoms are aligned in rows when it is viewed along the z-axis, wherein each cation alternates with the sulfur anions, which form a honeycomb structure in three dimensions (Fig. 2(d')).

The knowledge of the total energy of the system, or more often, the energy differences between the different phases may be useful for the understanding of many aspects of the crystalline behavior. Figure 3 shows the curve of total energy versus the formula unit (f.u.) volume for each phase fitted to the equation of state of Birch–Murnaghan.[34,35] Our calculations of the equilibrium energies showed that the energy ordering of the phases is ST > KS > WS > PMCA, which indicates that the ST phase is the most stable among them (see inset of Fig. 3). It is clearly seen that the total energy of the PMCA structure is higher than the others, which shows that it is the least stable.

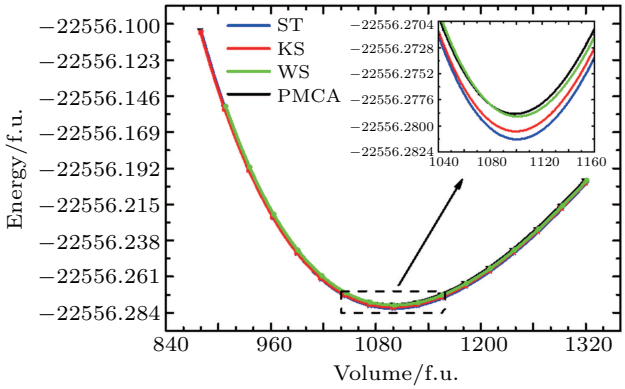


Fig. 3. (color online) Computed total energy (Ry) versus volume (a.u.) for the KS, ST, PMCA, and WS structures of the Cu_2MgSnS_4 compound.

The calculated values of the atomic coordinates, lattice constants, equilibrium volume, bulk modulus and its pressure derivative are summarized in Table 1 with other available results. For the KS and ST structures, the structural parameters are in good agreement with the available experimental or theoretical data.[27,29] For the other structures, to the best of our knowledge, no experimental or theoretical data are available for comparison. Thus, our results can serve as a prediction for future investigations.

Table 1. Equilibrium structural parameters (a (Å)), b/a, c/a, equilibrium volume/f.u. (V_0 (Å^3)) and atomic positions), bulk modulus (B), and its pressure derivative (B').

Phases	a/Å	b/a	c/a	V_0/Å^3	B/GPa	B'	Atomic positions				
							Atoms	site	x/a	y/b	z/c
KS	5.436	1	2.027	162.81	75.678	4.858	Cu(1)	2a	0	0	0
	5.427[a]	1[a]	1.999[a]	159.76[a]			Cu(2)	2c	0	0.5	0.25
							Mg	2d	0	0.5	0.75
							Sn	2b	0	0	0.5
							S	8g	0.2236 0.2433[a]	0.25025 0.24383[a]	0.12558 0.12822[a]
ST	5.505	1	1.954	162.99	76.128	4.850	Cu	4d	0	0.5	0.25
	5.568[b]	1[b]	1.963[b]	169.43[b]			Mg	2a	0	0	0
							Sn	2b	0	0	0.5
							S	8i	0.2508	0.2508	0.1384
PMCA	5.501	1	0.977	162.83	75.575	4.879	Cu	2f	0	0.5	0.5
							Mg	1a	0	0	0
							Sn	1d	0.5	0.5	0
							S	4n	0.2489	0.2489	0.2764
WS	7.749	0.856	0.818	162.91	75.811	4.863	Cu	4b	0.2495	0.1708	0.5159
							Mg	2a	0	0.6702	0.5184
							Sn	2a	0	0.3208	0.0179
							S(1)	4b	0.2492	0.1469	0.1575
							S(2)	2a	0	0.3157	0.6315
							S(3)	2a	0	0.6803	0.1300

[a]Ref. [27], [b]Ref. [29].

3.2. Elastic properties

We calculated the elastic stiffness tensors of the Cu_2MgSnS_4 compound, in order to analyse its mechanical stability for the KS, ST, PMCA, and WS phases. Due to the symmetry $C_{ij} = C_{ji}$, the total number of independent components (elastic constants) can be reduced from 36 to 21.[36] This number can be further reduced using the crystal symmetry to nine for the orthorhombic crystal structure, seven for KS phase and only six for ST and PMCA, the latter having tetragonal crystal structures. For the ST and PMCA which belong to the tetragonal Laue group TI, the expressions of the elastic moduli are well known, while for the KS belonging to the tetragonal Laue

group TII, they have not been derived analytically yet. This is due to the fact that the off-diagonal shear elastic constant C_{16} is not necessarily equal to zero. However, with regard to the elastic properties, separation of the tetragonal solids into the two Laue groups is not strictly required: in each case, the elastic stiffness tensor may be described in terms of six parameters. Indeed, with a rotation around the z-axis through a given angle by[37,38]

$$\phi = (1/4)\tan^{-1}(4C_{16}/C_{11} - C_{12} - 2C_{66}), \tag{1}$$

which transforms the C_{ij} to C'_{ij} as given in Ref. [39], where C'_{16} is equal to zero, reducing the number of independent elastic constants from seven to six for the KS structure. Equation (1) gives two values for ϕ in the range $\phi < |\pi/2|$ that correspond to ϕ_1 and ϕ_2, where $\phi_1 = \phi_2 + \pi/4$.[38,39] In our case we obtain $\phi_1 = 2.57°$, $\phi_2 = 47.57°$. The complete necessary and sufficient criteria of mechanical stability[40] for KS, ST, PMCA, and WS phases are

$$\begin{cases} C_{11} > |C_{12}|;\ 2C_{13}^2 < C_{33}(C_{11}+C_{12}), \\ C_{44} > 0;\ 2C_{16}^2 < C_{66}(C_{11}-C_{12}), \end{cases} \quad \text{for KS}, \tag{2}$$

$$\begin{cases} C_{11} > |C_{12}|;\ 2C_{13}^2 < C_{33}(C_{11}+C_{12}), \\ C_{44} > 0;\quad C_{66} > 0, \end{cases} \quad \text{for ST and PMCA}, \tag{3}$$

$$\begin{cases} C_{11} > 0;\ C_{11}C_{22} > C_{12}^2, \\ C_{11}C_{22}C_{33} + 2C_{12}C_{13}C_{33} - C_{11}C_{23}^2 \\ \quad - C_{22}C_{13}^2 - C_{33}C_{12}^2 > 0, \\ C_{44} > 0;\ C_{55} > 0;\ C_{66} > 0. \end{cases} \quad \text{for WS}. \tag{4}$$

The values of their independent elastic constants were estimated and are displayed in Table 2, which are positive and satisfy the above stability criteria. $C_{11} > C_{33}$ in the ST and PMCA phases implies that the bonding strength along the [100] and [010] direction is stronger than that of the bonding along the [001] direction, whereas the inverse trend is exhibited in WS and KS, since $C_{11} < C_{33}$ for both phases. $C_{44} < C_{66}$ in the ST and PMCA phases, suggesting that the [100] (010) shear is more difficult than the [100] (001) shear, while the inverse behavior is shown by the KS and WS phases since $C_{44} > C_{66}$.

We have calculated the universal elastic anisotropy index for all phases as follows: $A^{\mathrm{U}} = (5G_{\mathrm{V}}/G_{\mathrm{R}} + B_{\mathrm{V}}/B_{\mathrm{R}} - 6)$,[41] where we have found that the KS structure exhibits the most elastic anisotropy among them. We notice that for the tetragonal ones the elastic anisotropies are approximately the same. In order to calculate the values of the bulk moduli and shear moduli for polycrystalline materials, two main approximations are used: the Voigt and Reuss schemes.[42,43] The Voigt approximation is the upper limits of the above mentioned moduli, while the Reuss approximation corresponds to their lower limits. In addition, we have used the average of the Voigt and Reuss bulk and shear moduli, called the Voigt–Reuss–Hill (VRH) approximation,[44] to calculate Young's modulus (E), Lame's coefficient (λ), and Poisson's ratio (σ). The results are given in Table 2. Our calculation shows that the Young moduli of all the structures are rather close to one another (see Table 2), which show that they have almost the same stiffness. Based on Pugh's[45] empirical relationship, the B/G ratio can classify materials as ductile or brittle according to a critical value; if $B/G > 1.75$ the material is ductile, otherwise the material is brittle. The values calculated for B/G for all phases indicate that the Cu_2MgSnS_4 compound is prone to ductile behavior.

Table 2. Calculated elastic constants (C_{ij}, in GPa) and elastic parameters for Cu_2MgSnS_4 in four phases: bulk moduli (B_{V}, B_{R}, B_{VRH}, in GPa), shear moduli (G_{V}, G_{R}, G_{VRH}, in GPa), Pugh's indicator (B/G), Young's moduli (E, in GPa), Poisson's ratio (σ), Lame's constant (λ, in GPa), the elastic anisotropy indices (A^{U}).

C_{ij}	KS	ST	PMCA	WS
C_{11}/C'_{11}	93.522 / 93.368[a], 112.567[b]	95.200	95.968	110.553
C_{22}				104.669
C_{33}/C'_{33}	96.662 / 96.662[a,b]	93.196	93.765	127.539
C_{44}/C'_{44}	36.375 / 36.375[a,b]	32.616	33.555	22.489
C_{55}				18.140
C_{66}/C'_{66}	34.533 / 34.687[a], 15.488[b]	39.723	39.047	21.097
C_{12}/C'_{12}	62.238 / 62.392[a], 43.193[b]	66.066	66.160	56.621
C_{13}/C'_{13}	64.187 / 64.187[a,b]	62.494	62.860	47.647
C_{23}				51.621
C_{16}/C'_{16}	−1.713, 0[a,b]		0	
$B_{\mathrm{V}}, B_{\mathrm{R}}$	73.881, 73.819	73.967, 73.896	74.385, 74.316	72.726, 72.549
B_{VRH}	73.850	73.932	74.350	72.637
A^{U}	0.904	0.885	0.868	0.304
$G_{\mathrm{V}}, G_{\mathrm{R}}$	27.663, 23.429	27.160, 23.081	27.486, 23.424	24.803, 23.392
G_{VRH}	25.546	25.121	25.455	24.097
E	68.715	67.695	68.543	65.095
λ	56.819	57.184	57.380	56.573
σ	0.345	0.347	0.346	0.351
B/G	2.891	2.940	2.921	3.014

[a]Rotation angle of $\phi_1 = 2.57°$, [b]Rotation angle of $\phi_2 = 47.57°$.

3.3. Electronic properties

The calculated electronic band structures of Cu_2MgSnS_4 are shown in Fig. 4. The band structures of the four phases are quite similar. It can be seen that the KS, ST, and WS phases possess a direct band gap in the Γ–Γ direction of the Brillouin zone, while the PMCA phase has an indirect band gap in the Γ–A direction. The results are given in Table 3. We find that the energy gap is increased from the PMCA to the WS, while the KS and WS phases have nearly the same gap. The corrected band gaps according to the TB-mBJ calculation of KS and WS are 0.781 and 0.785 eV, respectively, while for ST it is 0.766 eV.

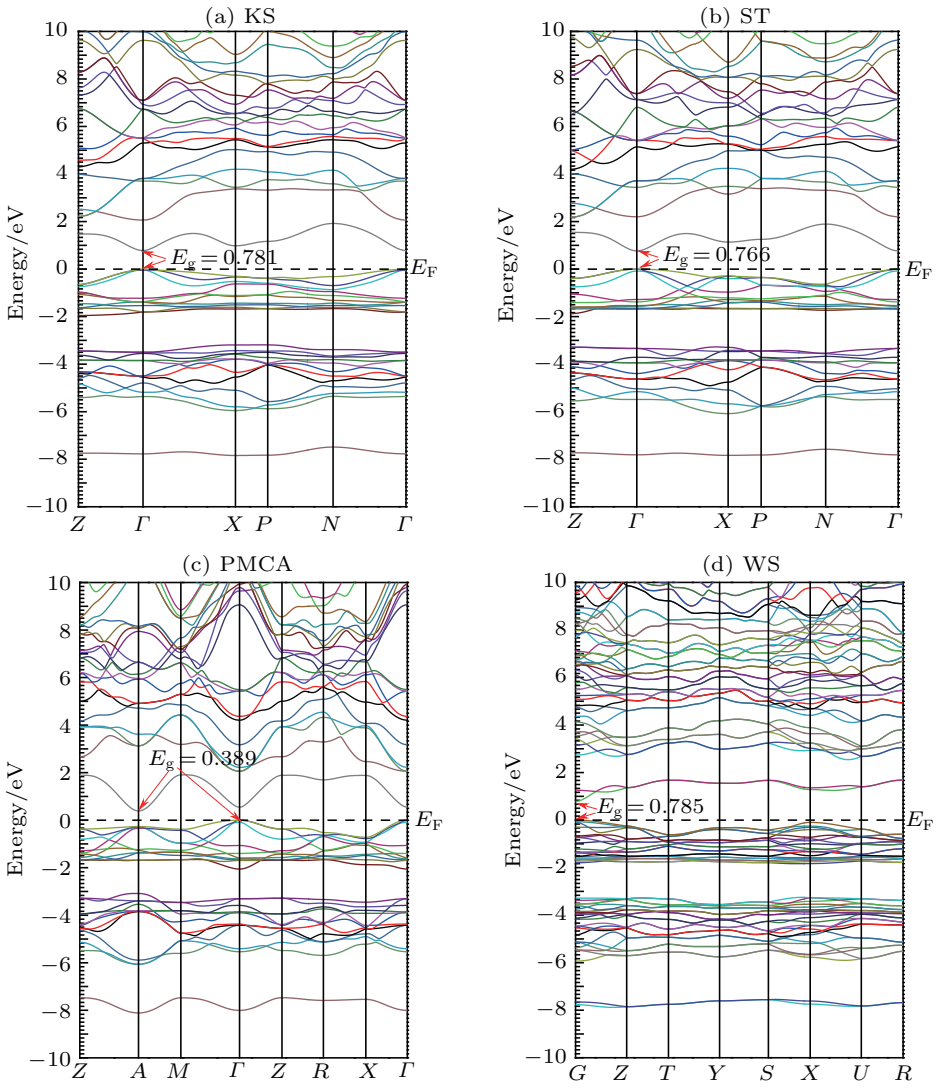


Fig. 4. (color online) Band structures along the principal high-symmetry directions in the Brillouin zone of Cu_2MgSnS_4 in (a) KS, (b) ST, (c) PMCA, and (d) WS phases.

The density of states (DOS) has an important role in the analysis of the physical properties of the materials. According to Fig. 5 of the total and partial DOS, we see that KS, ST, PMCA, and even WS have similar general features to each other. It is observed that the lower valence band in the energy ranging from −14.74 eV to −12.92 eV is mainly provided by the state S-s, and the upper valence band has three regions separated by gaps (labelled VBI, VBII, and VBIII): the first one from −8.05 to −7.37 is formed by a rather isolated band mainly provided by the S-sp, Sn-s states; the second one from −6.11 to −3.07 is dominated by the Cu-d, Sn-p, and S-p states; and the third one from −2.01 to 0 is strongly provided by Cu-d, less by S-p, and little contribution from Sn-sp. The gaps between VBI and VBII are 1.24, 1.40, 1.03, and 1.41 eV for KS, ST, PMCA, and WS, respectively, while the gaps between VBII and VBIII are 1.54, 1.50, 1.41, and 1.61 eV for KS, ST, PMCA, and WS, respectively. The conduction band in the range from 0.389 up to 15 eV has two regions separated by a gap of 0.14, 0.29, 0.15, and 0.86 eV for KS, ST, PMCA, and WS, respectively. The first one, labelled CBI, is formed by a quite isolated band that consists of a mixture of the Sn-s, S-p, S-s, and Cu-d states, while the second one, labeled CBII, extends from about 2 eV to high energies and is mostly composed of the Sn-p, S-p, S-s, and Cu-d states. The

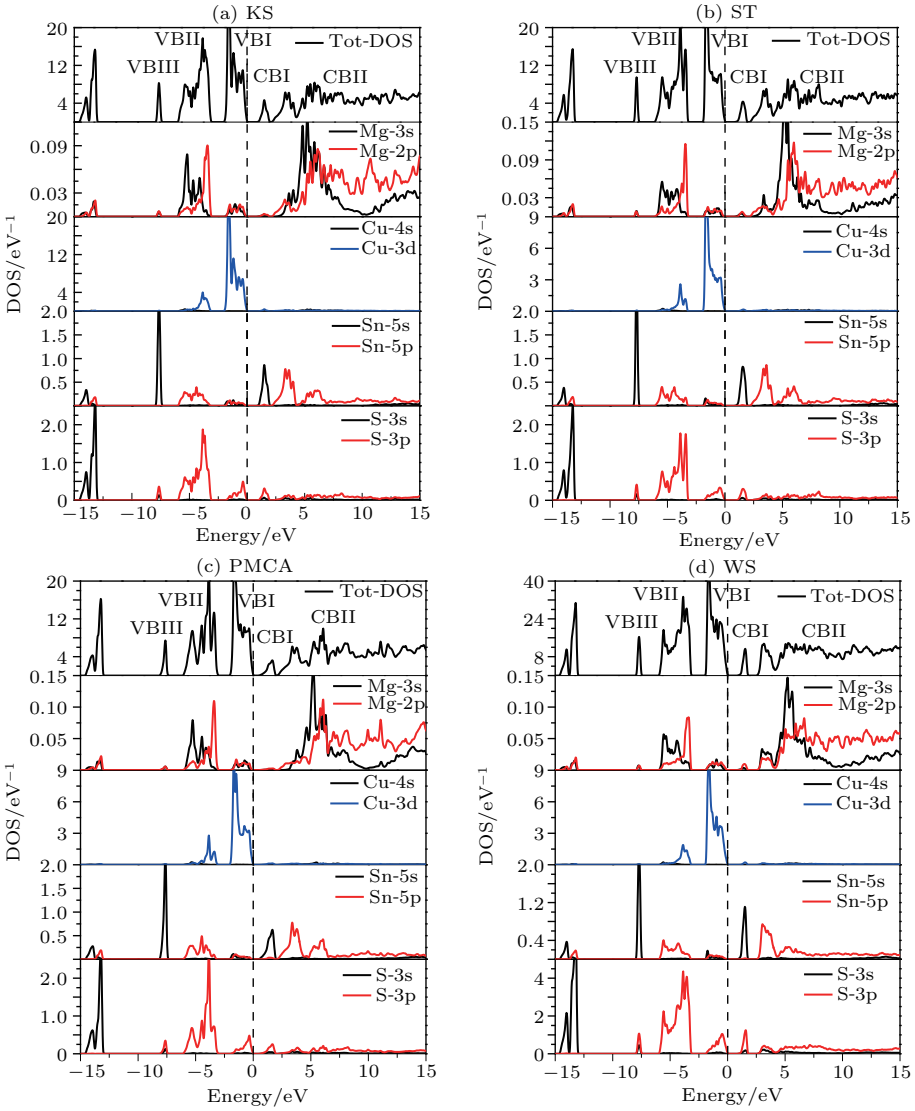


Fig. 5. (color online) Total and partial densities of states in (a) KS, (b) ST, (c) PMCA, and (d) WS phases.

Table 3. Band gaps of Cu_2MgSnS_4 in different phases.

Crystal structure	Fundamentals band gap/eV	Optical band gap/eV
KS	0.273* (GGA-PBEsol)	1.48* (TB-mBJ)
	0.781* (TB-mBJ)	1.63[a] (exp)
		1.76[b] (exp)
ST	0.239* (GGA-PBEsol)	1.61* (TB-mBJ)
	0.19[c] (GGA-PBE)	1.76[b] (exp)
	0.766* (TB-mBJ)	
	1.80[c] (HSE06)	
PMCA	0.015* (GGA-PBEsol)	
	0.389* (TB-mBJ)	
WS	0.281* (GGA-PBEsol)	1.77* (TB-mBJ)
	0.785* (TB-mBJ)	

[a]Ref. [27], [b]Ref [28], [c]Ref. [29], *Our work

top valence band is mainly the anti-bonding component of the p-d hybridization between the anion S and the cation Cu. The bottom conduction band is mainly the anti-bonding component of the s-s and s-p hybridization between the cation Sn and anion S with a significant contribution from the Cu-d state.

3.4. Optical properties

The complex dielectric function is defined as the three dimensional tensor $(\varepsilon^{\alpha\beta}(\omega) = \varepsilon_1^{\alpha\beta}(\omega) + i\varepsilon_2^{\alpha\beta}(\omega)$, where $\alpha, \beta = x, y$, or z) that can be used to describe the linear response of the system to electromagnetic radiation, which relates to the interaction of the photons and electrons. The calculations ignore the excitonic and local field effects. There are two contributions to $\varepsilon^{\alpha\beta}(\omega)$, namely the intra-band and inter-band transitions. The contribution from intra-band transitions is important only for metals. The inter-band transitions can further be split into direct and indirect transitions.

The indirect inter-band transitions which involved the scattering of phonons were ignored. The inter-band contribution to the imaginary part of the dielectric tensor components is calculated by summing transitions from occupied to unoccupied states over BZ, weighted with the appropriate momentum

matrix elements as given by[46]

$$\mathrm{Im}(\varepsilon^{\alpha\beta}(\omega)) = \frac{4\pi e^2}{m^2\omega^2}\sum_{i,f}\int \langle f|p_\alpha|i\rangle\langle i|p_\beta|f\rangle \times W_i(1-W_f)\delta(E_f-E_i-\hbar\omega)\mathrm{d}^3k, \quad (5)$$

where (e) is the electron charge, (m) is the mass, $\langle f|p_\alpha|i\rangle$ and $\langle i|p_\beta|f\rangle$ are the dipole matrix elements corresponding to the α and β directions of the crystal (x, y, or z), and f and i are the final and initial states, respectively. W_n is the Fermi distribution function for the nth state and E_n is the electron energy in the nth state. Since the dielectric function describes the causal response, the real and imaginary parts are linked using the Kramers–Kronig transform. Furthermore, the other energy-dependent optical parameters, such as the reflectivity $R^{\alpha\beta}(\omega)$, energy-loss function $L^{\alpha\beta}(\omega)$, and absorption coefficient $\alpha^{\alpha\beta}(\omega)$ can be derived from $\varepsilon_1^{\alpha\beta}(\omega)$ to $\varepsilon_2^{\alpha\beta}(\omega)$.[46] The PMCA phase is the least stable among the investigated phases and has an indirect band gap. Therefore, in this section, we will focus only on the other structures. The respective crystal symmetries imply that there are two components of the optical parameters tensors for the tetragonal (KS and ST) structures ($\varepsilon_i^{xx}(\omega) = \varepsilon_i^{yy}(\omega) = \varepsilon_i^{\parallel}(\omega)\varepsilon_i^{zz}(\omega) = \varepsilon_i^{\perp}(\omega)$) and three for the orthorhombic (WS) structure. We calculate the real $\varepsilon_1^{\alpha\alpha}(\omega)$ and imaginary $\varepsilon_2^{\alpha\alpha}(\omega)$ parts of the dielectric tensor in each direction, as shown in Fig. 6. We can see that they exhibit the same shape for the three phases over a broad range of energies. The tetragonal phases show an anisotropy between the two directions reflected by the behavior of the real parts $\varepsilon_1^{\alpha\alpha}(\omega)$ of their dielectric tensor as seen in Figs. 6(a) and 6(b). For the orthorhombic phase, the two lattice constants b and c along the y and z directions, respectively, are almost equal; consequently, the dielectric tensor components along these directions are close to each other as if it were a tetragonal structure ($\varepsilon_i^{yy}(\omega) \approx \varepsilon_i^{zz}(\omega)$, $\varepsilon_i^{\parallel}(\omega) = (\varepsilon_i^{yy}(\omega) + \varepsilon_i^{zz}(\omega))/2$ and $\varepsilon_i^{\perp}(\omega) = \varepsilon_i^{xx}(\omega)$), while a clear anisotropy is exhibited between the x and both these directions as seen in Fig. 6(d).

The onsets of the calculated $\varepsilon_2(\omega)$ spectra corresponding to their first optical critical points occur at 0.785 eV for the three components of the WS phase, 0.766 and 0.781 eV for both components of the ST and KS phases, respectively, which correspond to the threshold of direct optical transition between the highest valence band maximum and the lowest conduction band minimum at the Γ point for all phases, in good agreement with their respective fundamental band gaps. Beyond these points, the curves present several peaks. In particular, the $\varepsilon_2^{\alpha\alpha}(\omega)$ along each direction for all phases has five more pronounced peaks around 1.7–9.5 eV, labeled A, B, C, D, and E. The highest peaks positions are at around 7.17, 7.04, and 6.98 eV for the KS, ST, and WS phases, respectively. The peaks (A) can be assigned to the transitions from Cu-3d/S-3p states of VBI to the Sn-5s/S-3p states of CBI. The peaks (B, C) can be attributed to the transitions from Cu-3d/S-3p states of VBI to Sn-5p/Cu-3d/S-3p states of CBII, the peaks (D) may correspond mainly to the transitions from S-3p/Sn-5p/Cu-4s states of VBII to Sn-5s/S-3p of CBI states, and the peaks (E) may be due to the transitions from S-3p/Sn-5p/Cu-3d states of VBII to Sn-5p/Cu-4s/S-3p states of CBII. It is noted that the peak in $\varepsilon_2(\omega)$ does not correspond to a single interband transition since many transitions may be found in the band structure with an energy corresponding to the same peak.

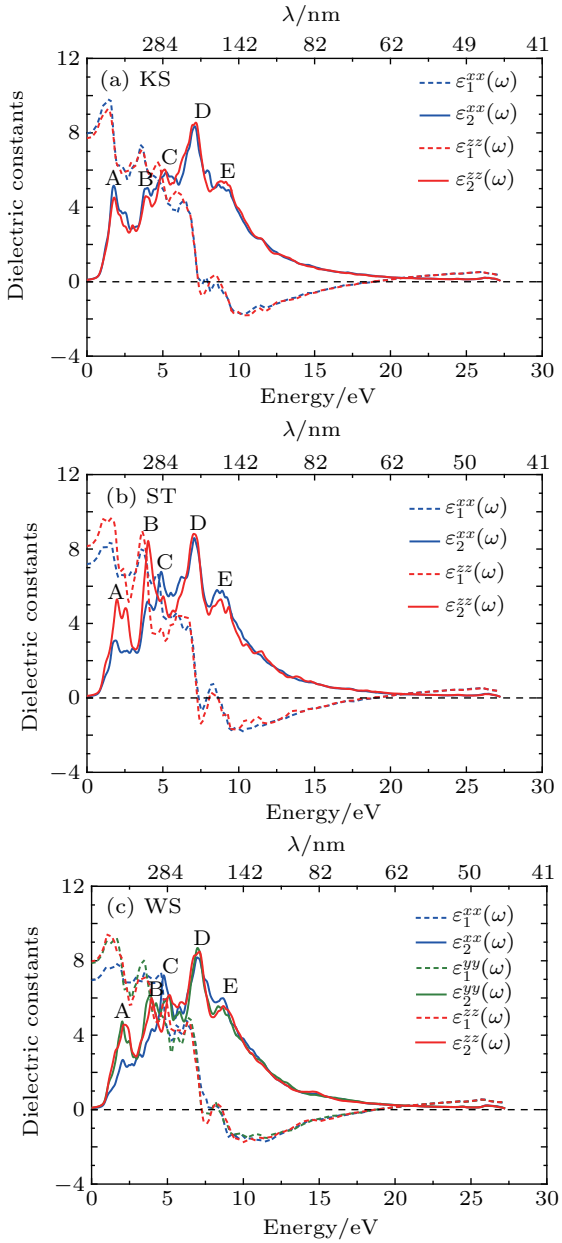


Fig. 6. (color online) The real and imaginary parts of the dielectric function for Cu_2MgSnS_4 in (a) KS, (b) ST, and (c) WS phases along crystallographic directions.

For the realpart spectrum, the main peaks (with magnitudes 9.81 and 9.29 for $\varepsilon_1^{xx}(\omega)$ and $\varepsilon_1^{zz}(\omega)$, respectively) for the KS phase are situated around 1.40–1.51 eV; for the ST phase they are located around 1.55–1.62 eV (8.38 and 9.65 for $\varepsilon_1^{xx}(\omega)$, and $\varepsilon_1^{zz}(\omega)$ respectively); for the WS phase they occur

at 1.1–1.63 eV (7.82, 9.18, and 9.42 for $\varepsilon_1^{xx}(\omega)$, $\varepsilon_1^{yy}(\omega)$, and $\varepsilon_1^{zz}(\omega)$, respectively). We can see that the dielectric functions for the ST and WS phases display maximum anisotropy in the energy range 0–5.7 eV. The spectra curve of each $\varepsilon_1^{\alpha\alpha}(\omega)$ crosses the zero line four times for the KS and ST phases, and also for the WS phase, except for its $\varepsilon_1^{xx}(\omega)$ component, which crosses the zero line twice. The $\varepsilon_1^{\alpha\alpha}(\omega) = 0$ is a necessary condition for plasma oscillations to occur but not a sufficient condition.[47] Thus, the corresponding screened plasma frequencies[48] will be determined from the analysis of the electron energy-loss function. Furthermore, the static dielectric constants near zero photon energy can be easily obtained as $\varepsilon_1^{xx}(0) = 7.97$, $\varepsilon_1^{zz}(0) = 7.71$ for KS, $\varepsilon_1^{xx}(0) = 7.19$, $\varepsilon_1^{zz}(0) = 8.16$ for ST and $\varepsilon_1^{xx}(0) = 6.95$, $\varepsilon_1^{yy}(0) = 7.87$, $\varepsilon_1^{zz}(0) = 7.97$ for WS. For the three phases, the directionally averaged values of the zero frequency dielectric constants $\varepsilon_1(0)$ are 7.88, 7.51, and 7.60 for KS, ST, and WS, respectively. The uniaxial anisotropies $\delta\varepsilon = (\varepsilon_1^{\parallel}(0) - \varepsilon_1^{\perp}(0))/\varepsilon_1(0)$ are 0.033, −0.129, and 0.128 for KS, ST, and WS, respectively. These values confirm the existence of the anisotropy for these phases. Furthermore, the WS and ST phases show a noticeable anisotropy compared to the KS phase. On the other hand, in the absence of experimental data on the polarized zero frequency dielectric constant, no comment can be ascribed to the accuracy of our results.

The surface behavior of a material is characterized by its reflectivity $R(\omega)$, which is defined as the ratio of the incident power to the reflected power. Figure 7 displays the energy dependence of the different reflectivity components for the three phases up to 27 eV. We can see that they exhibit the same shape. Indeed, in the low energy range below 2.5 eV, isolated peaks occur and several peaks appear in the broad energy range 2.5–20 eV. The zero-frequency reflectivities are $R^{xx}(0) = 22.7\%$, $R^{zz}(0) = 22.1\%$ for KS, $R^{xx}(0) = 20.9\%$, $R^{zz}(0) = 23.2\%$ for ST and $R^{xx}(0) = 20.3\%$, $R^{yy}(0) = 22.5\%$ and $R^{zz}(0) = 22.7\%$ for WS. The maximum reflectivities for KS (44.20%), ST (42.37%), and WS (44.84%) correspond to 12.00, 12.62, and 11.94 eV respectively. It is worth underlining that the reflectivity along each direction $R^{\alpha\alpha}(\omega)$ reaches its maximum value when its corresponding $\varepsilon_1^{\alpha\alpha}(\omega)$ is below zero. For negative values of $\varepsilon_1(\omega)$, the materials are characterized as metals.[49]

The electron energy-loss function describes the interaction by which energy is lost by a fast moving electron traveling the material. The sharp peaks of our calculated energy-loss function (Fig. 8) have maxima at 19.69, 19.43, and 19.40 eV for KS, ST, and WS, respectively, corresponding to their screened plasma frequencies above which the matter acts as a dielectric and below which it shows a metallic nature, in agreement with the last root of their respective $\varepsilon_1(\omega)$ ($\varepsilon_1(\omega) = 0$) and fits very well with the rapid decrease in reflectivity in

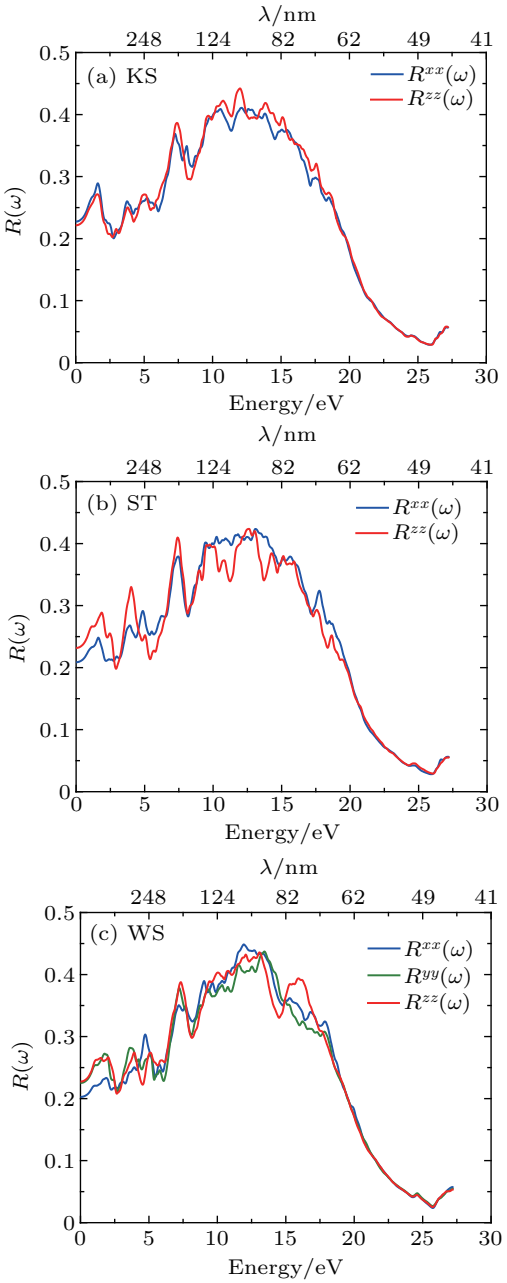


Fig. 7. (color online) Optical reflectivity for Cu_2MgSnS_4 in (a) KS, (b) ST, and (c) WS phases along crystallographic directions.

Fig. 7.

The optical absorption coefficient $\alpha(\omega)$ is one of the most crucial evaluation criteria for the optical properties. Figure 9 displays the energy dependence of the absorption coefficient in each direction for the three phases up to 27 eV. Overall, they have similar absorption spectra. Indeed, they grow for photon energies higher than 1.47, 1.56, and 1.76 eV for KS, ST, and WS structures, respectively, which means these phases start absorbing the radiation at wavelengths below 844, 795, and 705 nm, respectively. In addition, the region of intense absorption starts from these onsets to about 27 eV. The above mentioned energy regions consist of different spectral peaks occurring due to different electronic transitions where the highest peaks occur at 10.25, 9.83, and 11.44 eV for KS, ST, and WS

structures, respectively, corresponding to an abrupt decrease of the $\varepsilon_2(\omega)$ shown in Fig. 6. In particular, the absorption in the visible region exceeds 10^{-4} cm^{-1}, which shows that this compound is a potential photovoltaic absorber.

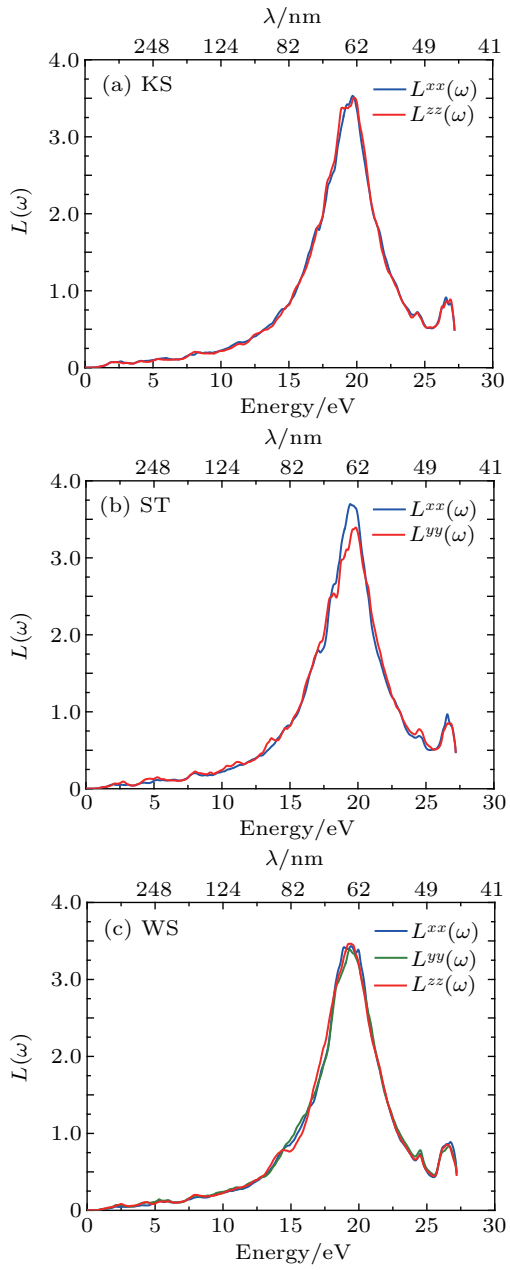


Fig. 8. (color online) Electron energy-loss spectrum for Cu_2MgSnS_4 in (a) KS, (b) ST, and (c) WS phases along crystallographic directions.

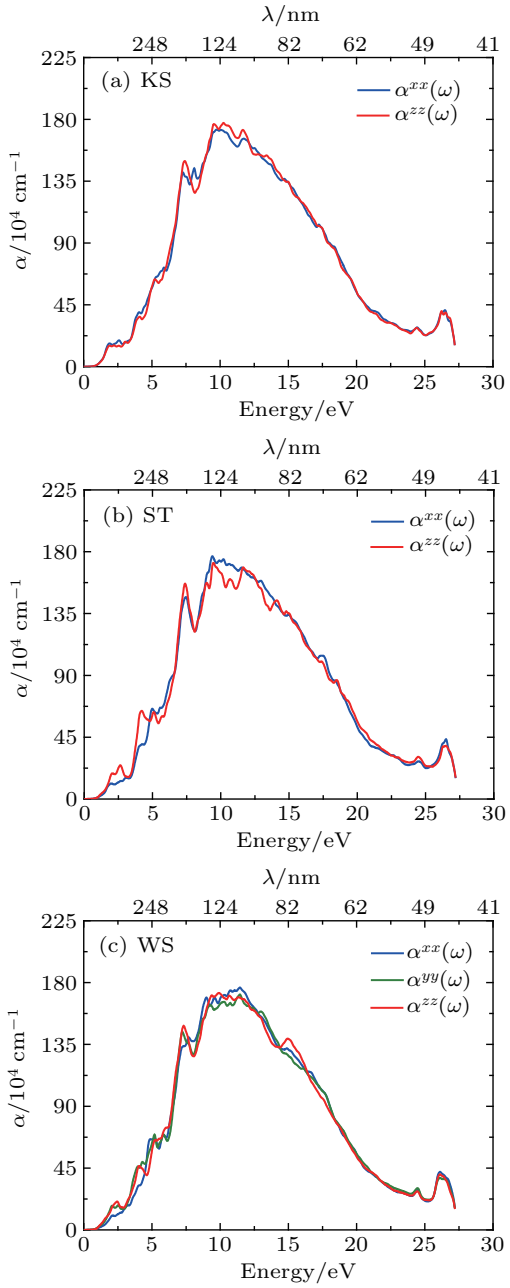


Fig. 9. (color online) Absorption coefficient for Cu_2MgSnS_4 in (a) KS, (b) ST, and (c) WS phases along crystallographic directions.

Since the available experimental band gap of this compound is determined optically by the UV–vis diffuse reflectance spectroscopy,[27] and it is well known that when the excitonic effects are neglected the fundamental band gap is usually smaller than the optical band gap, which can be due to dipole-forbidden transitions or weak (optical) transition matrix elements. It is important to keep in mind that the fundamental band gap is the smallest energy which allows electrons to be excited in unoccupied states. In contrast, the optical band gap is related to an excitation using photons. Thus, we should take into account the difference between the two band gap concepts when comparing the theoretical results with the corresponding experimental data.

Unfortunately, the optical band gap is not reported in the Ref. [29] using the screened hybrid HSE06 functional approach, but we can expect that this approach overestimates the optical band gap based on the fact that the HSE06 fundamental band gap (1.80 eV) is higher than the experimental optical band gap (1.63 and 1.76 eV).[27,28] Figure 10 shows $(\alpha h\nu)^2$ versus $(h\nu)$ where (α) is the directionally averaged optical absorption coefficient calculated with the TB-mBJ for the three phases at low energies up to 3.5 eV, from which the opti-

cal band gap energies of Cu_2MgSnS_4 are estimated through Tauc's plot method.[50] The estimated TB-mBJ optical band gap of the KS structure agrees with the experiment. Additionally, when comparing the TB-mBJ optical band gaps, we found that they decrease, going from the WS phase to the KS phase.

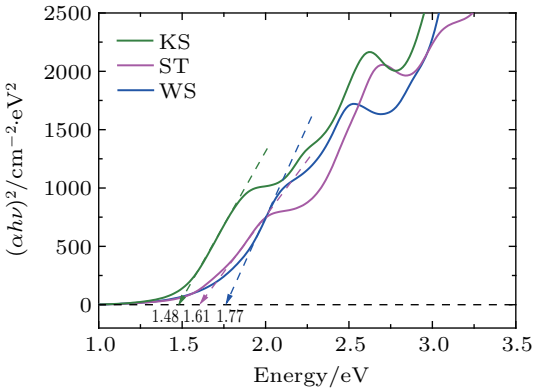


Fig. 10. (color online) Determination of optical band gap of Cu_2MgSnS_4 using TB-mBJ for KS, ST, and WS phases.

4. Conclusion

In the present work, the structural, elastic, electronic, and optical properties of Cu_2MgSnS_4 have been investigated using the FP-LAPW+lo method within the GGA PBEsol in the framework of the DFT. Our calculations for the Cu_2MgSnS_4 in different phases, namely KS, ST, PMCA, and WS, show that the ST phase is the most stable among them. The calculated structural parameters of the KS phase are in reasonable agreement with the available experimental and theoretical results. From our calculated elastic constants for the different phases this material is mechanically stable, could be classified as a ductile material, and the KS structure exhibits the highest elastic anisotropy. On the other hand, following Pugh's empirical relationship, Cu_2MgSnS_4 behaves in a ductile manner for all phases. According to the TB-mBJ calculation, Cu_2MgSnS_4 exhibits a semiconducting behavior with an indirect band gap in the M–A direction for the PMCA phase and a direct band gap in the Γ–Γ direction for the others.

For the optical properties, it is found that the TB-mBJ calculation gives more reliable results than the other approaches. In particular, the estimated optical band gaps of the KS and ST phases are in agreement with the experimental results. To the best of our knowledge, there have not been any previous theoretical results on the electronic and optical properties of Cu_2MgSnS_4 in the wurtzite–stannite phase, including the dielectric function, the absorption coefficient, the reflectivity, and the energy-loss function. Therefore, we hope that our results could serve as a reference for future studies. Currently, the best performing thin-film solar cells on the cellular as well as on the module-level are fabricated using $Cu(Ga,In)Se_2$ absorbers. Despite having superior efficiencies, they present limitations arising from the cost and/or scarcity of Ga and In. Therefore, one major challenge for thin-film photovoltaic technology is to develop materials composed of earth-abundant and nontoxic elements. Cu_2MgSnS_4 which is structurally similar to chalcopyrite semiconductors, such as $CuGaSe_2$, $CuInSe_2$, and $Cu(Ga,In)Se_2$, but contains only earth-abundant, nontoxic elements and has a near optimal direct band-gap energy of $E_g \sim 1.5$ eV with high optical absorption coefficients, can be a potential candidate for high-efficiency application in low-cost solar cells, with the same device design, structure, and processing as chalcopyrite solar cells. Moreover, from the DOS analysis, the band-gap energy can be tailored by cation alloying for an optimized optical efficiency of the materials.

References

[1] Ford G M, Guo Q, Agrawal R and Hillhouse H W 2011 *Chem. Mater.* **23** 2626
[2] Shi X Y, Huang F Q, Liu M L and Chen L D 2009 *Appl. Phys. Lett.* **94** 122103
[3] McCabe G H, Fries T, Liu M T, Shapira Y, Ram-Mohan L R, Kershaw R, Wold A, Fau C, Averou M and McNiff E J 1997 *Phys. Rev. B* **56** 6673
[4] Honig E, Shen H S, Yao G Q, Doverspike K, Kershaw R, Dwight K and Wold A 1988 *Materials Research Bulletin* **23** 307
[5] Guo Q, Ford G M, Yang W C, Walker B C, Stach E A, Hillhouse H W and Agrawal R 2010 *J. Am. Chem. Soc.* **132** 17384
[6] Goetzberger A, Hebling C and Schock H W 2003 *Mater. Sci. Eng: Rep.* **40** 1
[7] Medina S, Bouhafs B and Ruterana P 2014 *Computational Materials Science* **85** 159
[8] Ghosh A, Thangavel R and Rajagopalan M 2014 *Energy and Environment Focus* **3** 142
[9] Levcenco S, Dumcenco D, Huang Y S, Arushanov E, Tezlevan V, Tiong K K and Du C H 2011 *J. Alloy. Compound.* **509** 7105
[10] Li Y, Fan W, Sun H, Cheng X, Li P and Zhao X 2011 *J. Phys.: Conden. Matt.* **23** 225401
[11] Liu M L, Chen I W, Huang F Q and Chen L D 2009 *Adv. Mater.* **21** 3808
[12] Sevik C and Çaağın T 2010 *Phys. Rev. B* **82** 045202
[13] Hirai T, Kurata K and Takeda Y 1967 *Solid-State Electron.* **10** 975
[14] Chen S, Gong X G, Walsh A and Wei S H 2009 *Phys. Rev. B* **79** 165211
[15] Chen S, Walsh A, Luo Y, Yang J H, Gong X G and Wei S H 2010 *Phys. Rev. B* **82** 195203
[16] Hersh P A 2007 *Wide Band Gap Semiconductors and Insulators: Synthesis, Processing, and Characterization* (PhD thesis) (Oregon State University) http://ir.library.oregonstate.edu/xmlui/handle/1957/7422
[17] Wang X, Li J, Zhao Z, Huang S and Xie W 2012 *J. Appl. Phys.* **112** 02370
[18] Wang C C, Chen S Y, Yang J H, Lang L, Xiang H J, Gong X G, Walsh A and Wei S H 2014 *Chem. Mater.* **26** 3411
[19] Mitzi D B, Gunawan O, Todorov T K, Wang K and Guha S 2011 *Solar Energy Materials and Solar Cells* **95** 1421
[20] Chen S, Gong X G, Duan C G, Zhu Z Q, Chu J H, Walsh A, Yao Y G, Ma J and Wei S H 2011 *Phys. Rev. B* **83** 245202
[21] Zhang Y, Yuan X, Sun X, Shih B C, Zhang P and Zhang W 2011 *Phys. Rev. B* **84** 075127
[22] Ocheretova V A, Parasyuk O V, Fedorchuk A O and Khyzhun O Y 2015 *Mater. Chem. Phys.* **160** 345
[23] Chen D and Ravindra N M 2013 *J. Alloy. Compound.* **579** 468
[24] Himmrich M and Haeuseler H 1991 *Spectrochimica Acta Part A: Molecular Spectroscopy.* **47** 933
[25] Chen Y S, Wang Y J, Li R, Gu J H, Lu J X and Yang S E 2012 *Chin. Phys. B* **21** 058801
[26] Li Y M, Qiu L X, Ding Z H, Li Y F, Yao B, Xiao Z Y and Zhu P W 2016 *Chin. Phys. Lett.* **33** 076101

[27] Wei M, Du Q, Wang R, Jiang G, Liu W and Zhu C 2014 *Chem. Lett.* **43** 1149
[28] Guo Y, Cheng W, Jiang J, Zuo S, Shi F and Chu J 2016 *Mater. Lett.* **172** 68
[29] Zhong G, Tse K, Zhang Y, Li X, Huang L, Yang C, Zhu J, Zeng Z, Zhang Z and Xiao X 2016 *Thin Solid Film.* **603** 224
[30] Perdew J P, Ruzsinszky A, Csonka G I, Vydrov O A, Scuseria G E, Constantin L A, Zhou X and Burke K 2008 *Phys. Rev. Lett.* **100** 136406
[31] Tran F and Blaha P 2009 *Phys. Rev. Lett.* **102** 226401
[32] Koller D, Tran F and Blaha P 2012 *Phys. Rev. B* **85** 155109
[33] Blaha P, Schwarz K, Madsen G K H, Kvasnicka D and Luitz J 2016 *WIEN2K, an Augmented Plane Wave + Local Orbitals Program for Calculating Crystal Properties* Ed Schwarz K (Wien: Technische Universität Austria)
[34] Muranghan F D 1944 *Proc. Natl. Acad. Sci.* **30** 244
[35] Birch F 1947 *Phys. Rev.* **71** 809
[36] Nye J F 1985 *Physical Properties of Crystals: their Representation by Tensors and Matrices* (Oxford University Press)
[37] Blanchfield P and Saunders G A 1979 *J. Phys. C: Solid State Phys.* **12** 4673
[38] Farley J M, Saunders G A and Chung D Y 1973 *J. Phys. C: Solid State Phys.* **6** 2010
[39] Farley J M and Saunders G A 1972 *J. Phys. C: Solid State Phys.* **5** 3021
[40] Mouhat F and Coudert F X 2014 *Phys. Rev. B* **90** 224104
[41] Ranganathan S I and Ostoja-Starzewski M 2008 *Phys. Rev. Lett.* **101** 055504
[42] Voigt W 1928 *Lehrbuch der Kristall-physik*, 2nd ed. (Leipzig: Teubner Press)
[43] Reuss A 1929 *Z. Angew. Math. Mech.* **9** 49
[44] Hill R 1952 *Proceedings of the Physical Society Section A* **65** 349
[45] Pugh S F, XCII 1954 *The London, Edinburgh, and Dublin Philosophical Magazine and Journal of Science* **45** 823
[46] Ambrosch-Draxl C and Sofo J O 2006 *Comput. Phys. Commun.* **175** 1
[47] Nasr T B 2011 *Physica B: Condensed Matter.* **406** 287
[48] Wooten F 1972 *Optical Properties of Solids* New York and London
[49] Xu B, Li X, Sun J and Yi L 2008 *The European Physical Journal B* **66** 483
[50] Yakuphanoglu F 2011 *Solar Energy* **85** 2518